Progress In Electromagnetics Research, Vol. 143, 67–86, 2013

COMPACT ELECTROMAGNETIC ABSORBERS FOR FREQUENCIES BELOW 1 GHz

Rodolfo Araneo*, Giampiero Lovat, and Salvatore Celozzi

Electrical Engineering Division of DIAEE, University of Rome "La Sapienza", Via Eudossiana, Rome 18-00184, Italy

Abstract—A novel Frequency Selective Surface (FSS) configuration is proposed for the design of polarization-insensitive metamaterial absorbers operating below 1 GHz, where the first resonances of small commercial enclosures appear. The novel FSS shows a strong sub-wavelength response, enhanced by the dielectric substrate, which allows the design of compact planar absorbers with excellent angular and polarization stability.

1. INTRODUCTION

In the electromagnetic (EM) shielding practice, metallic enclosures are widely used to minimize unwanted emissions from noisy sources and to improve the immunity of susceptible equipments against external EM fields [1–4]. The shielding effectiveness (SE) [2, 5–7] of a cabinet is usually quantified in the frequency domain according to the IEEE Std. 299: It is computed as the ratio between incident and shielded electric (or magnetic) fields at a given position inside the enclosure. Recently, alternative integral [8, 9] and time-domain definitions [10] have been proposed too. The screening performance of a metallic enclosure can be dramatically degraded in presence of cavity resonances, because of the excitation of internal modes enhancing the EM field at given positions. Consequently, in dealing with practical enclosures having openings along their sides, the amount of EM field leaking into (or exiting from) the enclosure can be greatly increased in the proximity of such resonant frequencies [3, 5]. Therefore, it is a common practice to line internal surfaces of cabinets with properly designed absorbers in order to damp resonances [11–13].

Received 2 July 2013, Accepted 21 October 2013, Scheduled 28 October 2013

* Corresponding author: Rodolfo Araneo (rodolfo.araneb@uniroma1.it).

Frequency Selective Surfaces (FSSs) have been extensively studied in a number of applications and frequency ranges [14, 15]: their generally sharp frequency selective behaviour is well known and often exploited as a positive characteristic, but in several circumstances a large bandwidth is required and performance insensitive to angle of incidence and polarization of the incident plane wave field are pursued [16, 17]. Recently [18], the EM behaviour of FSSs has been investigated against near-field sources.

In this work, a novel intertwined spiral-aperture FSS is proposed as a possible candidate for the design of absorbers for damping the first resonant modes inside commercial shielded enclosures (e.g., desktop computer cases), whose resonant frequencies are usually below 1 GHz. The EM behaviour of the proposed FSS is characterized in terms of the reflection coefficient against incident plane waves: resonant frequencies, bandwidth (BW), fractional bandwidth (FBW), and polarization stability in a broad range of incidence angles are studied. Finally, an absorbing material based on the proposed FSS is proposed and analysed in terms of its absorption capabilities.

In the Appendix, it is shown how the proposed FSS configuration may be adapted to conform to apertures in actual enclosures configurations.

2. DESCRIPTION OF THE PROBLEM

The EM problem under analysis is sketched in Fig. 1(a): a perfectly conducting metallic enclosure with dimensions $a \times b \times c$, with an aperture on one of its sides, is illuminated by an impinging external field $\mathbf{E}^{\text{inc}} = 1\,\text{V/m}$, which excite internal resonances deteriorating the shielding performance of the cabinet. As an example, in Fig. 1(b) the electric field SE_E is reported for a common enclosure with dimensions $30 \times 40 \times 12\,\text{cm}$, with a rectangular $15 \times 3\,\text{cm}$ aperture on its front side. The results are achieved by means of a Method of Moments (MoM) formulation [18–20] in the frequency range between 100 MHz and 1 GHz. The aperture is illuminated with a normally-impinging uniform plane wave with the electric field linearly polarized along the shortest side of the aperture and the observation point is located at the center of the enclosure.

It is evident that resonances and anti-resonances of the SE_E take place in the considered frequency range: they depend on the position of the observation point inside the cavity and on the resonant modes excited by the field source. Fig. 1(c) shows the maps of the magnitude of the electric field in planes passing through the center of the enclosure, at the first resonant frequency $f = 615\,\text{MHz}$. It is

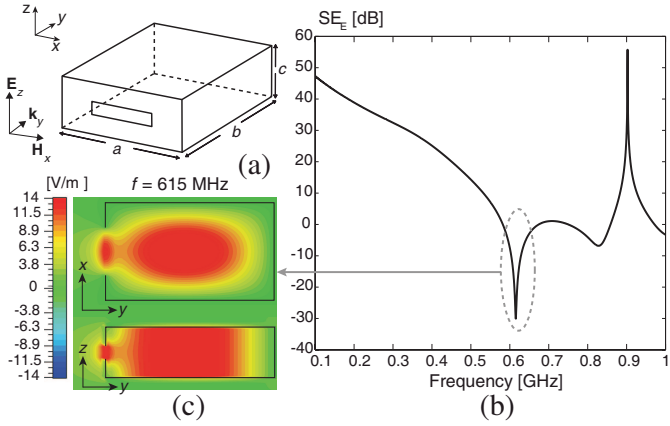

Figure 1. (a) Shielding enclosure illuminated by an impinging plane wave; (b) shielding effectiveness of the enclosure; (c) maps of the magnitude of the electric field at the first resonant frequency $f = 615\,\text{MHz}$.

easy to note that the first resonant mode of the enclosure is excited, which gives rise to a peak of electric field at the center of the enclosure where the observation point is placed, and, consequently, causes the antiresonance that is observable in the frequency trend of the SE_E.

In order to improve the SE_E, especially in the neighbourhood of the resonant frequencies, the interior surfaces of the cabinet are lined with an artificial absorbing material adequately designed.

3. INTERTWINED SPIRAL-APERTURE FSS

Recently, a new topology of planar FSSs composed of entwined quadrifilar spirals has been proposed [21]: as shown in Fig. 2(a), it is formed by the tessellation of a basic spiral with four arms protruding from the reference unit cell into the gaps between the turns of four spirals lying in the four adjacent unit cells. It should be noted that the externally protruding arms are counter-wounded with respect to the adjacent spiral arms. This type of element provides a very compact unit-cell size, showing a strong sub-wavelength response at dimensions smaller than 1/40 of wavelength, and has demonstrated a stable response to both TE and TM waves incident at different angles [22]. The novel FSS here proposed is based on the dual structure represented by an entwined quadrifilar spiral array (i.e., an *intertwined spiral-aperture array*). In fact, the resulting structure shown in Fig. 2(a)

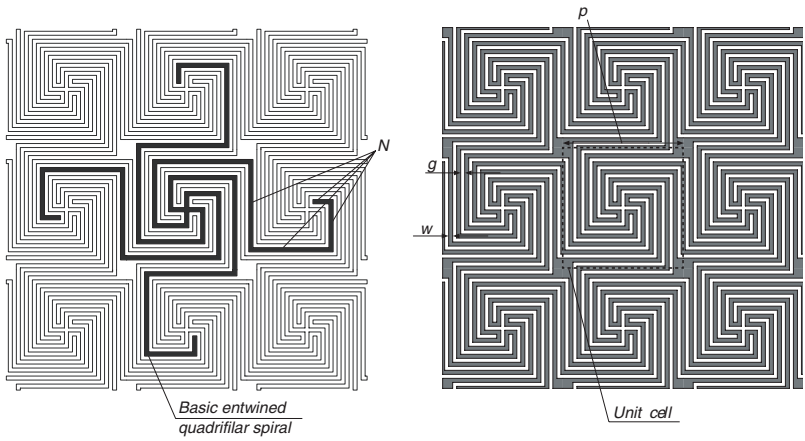

Figure 2. (a) Doubly periodic array of entwined quadrifilar spirals and (b) dual structure of entwined spiral apertures.

consists of an electrically continuous surface with a doubly periodic array of entwined quadrifilar spiral apertures. The reflection coefficient of this structure exhibits improved performance in terms of resonant frequency and fractional bandwidth, providing compact unit cell sizes. The geometrical parameters of the quadrifilar spiral-aperture surface are the period p, the strip width w, the spacing g, and the number of counter-wound spiral segments N, as shown in Fig. 2(b).

4. INTEGRAL EQUATION FORMULATION AND SOLUTION

The considered EM problem can be described and efficiently solved by means of a full-wave integral equation approach.

We consider an FSS represented by identical metallic objects of arbitrary shape, periodically arranged in the xy-plane. Without loss of generality, we assume that the periodic structure has skew axes $x = 0$ and $y = x \tan \phi$, with spatial periods p_y and p_s, respectively. The FSS is illuminated by a plane wave impinging with incidence angles ϕ_i and θ_i measured according to a spherical reference coordinate system. The structure, together with the geometrical and physical quantities, is shown for clarity in Fig. 3. The electric field $\mathbf{E}^{\text{inc}}$ of the incident plane wave is

$$\mathbf{E}^{\text{inc}} = E^{\text{inc}} \left[\mathbf{u}_\theta \cos(\alpha) + \mathbf{u}_\phi \sin(\alpha) \right] \mathrm{e}^{j\, \mathbf{k}^{\text{inc}} \cdot \mathbf{r}} \tag{1}$$

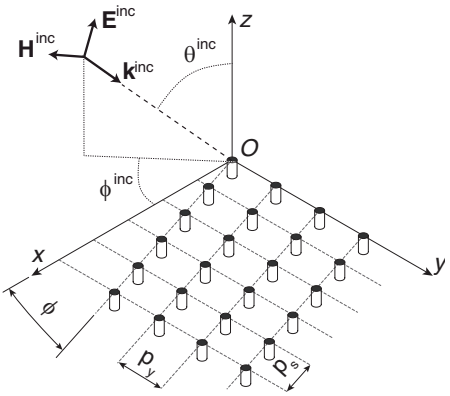

Figure 3. Sketch of a general 3-D problem with 2-D periodicity along skewed axes. The particular case of two perpendicular axes can be obtained setting the angle $\phi = 0$.

where E^{inc} is the plane-wave amplitude, α is the real polarization angle, and the wave vector is

$$\mathbf{k}^{\text{inc}} = \mathbf{u}_x k_x^{\text{inc}} + \mathbf{u}_y k_y^{\text{inc}} + \mathbf{u}_z k_z^{\text{inc}} \ , \tag{2}$$

being

$$\begin{aligned} k_x^{\text{inc}} &= -k_0 \sin\left(\theta^{\text{inc}}\right) \cos\left(\phi^{\text{inc}}\right) \\ k_y^{\text{inc}} &= -k_0 \sin\left(\theta^{\text{inc}}\right) \sin\left(\phi^{\text{inc}}\right) \\ k_z^{\text{inc}} &= -k_0 \cos\left(\theta^{\text{inc}}\right) \ , \end{aligned} \tag{3}$$

where $k_0 = \omega\sqrt{\mu_0 \epsilon_0}$ is the free-space wavenumber and $\mathbf{r} = \mathbf{u}_x x + \mathbf{u}_y y + \mathbf{u}_z z$ defines the observation point.

Thanks to the two-dimensional (2-D) periodicity of the structure and to the pseudo-periodic nature of the plane-wave excitation, based on Floquet's theorem [23], only one spatial period (unit cell) needs to be considered. In particular, the current induced on the conductive regions can be calculated by solving the relevant electric-field integral equation (EFIE):

$$\mathbf{u}_n \times \left[\mathbf{E}^{\text{inc}} + \mathbf{E}^{\text{s}}\left(\mathbf{J}\right)\right] = \mathbf{0} \quad \text{on } S \tag{4}$$

where $\mathbf{E}^{\text{inc}}$ is the incident field of the incoming plane wave, $\mathbf{E}^{\text{s}}\left(\mathbf{J}\right)$ is the scattered field due to the unknown induced electric current density $\mathbf{J}$ on the PEC elements, and $\mathbf{u}_n$ is the unit vector normal to the surface S of the elements within the unit cell. The EFIE in (4) can be solved more efficiently in a mixed-potential (MPIE) form [24]: by introducing

the magnetic vector potential $\mathbf{A}$ and the electric scalar potential V, the scattered electric field can be expressed as

$$\begin{aligned}\mathbf{E}^{\mathrm{s}} &= \int_S \left(- j\omega\mathbf{A} - \nabla V \right) \mathrm{d}S' \\ &= -j\omega \int_S \underline{\mathbf{G}}_A \cdot \mathbf{J} \, \mathrm{d}S' + \frac{1}{j\omega} \int_S \nabla \left(G_V \, \nabla \cdot \mathbf{J} \right) \mathrm{d}S' \end{aligned} \tag{5}$$

where $\underline{\mathbf{G}}_A$ and G_V are the potential periodic Green's functions for a 2-D periodic array of electric dipoles and electric charges in free space, respectively. The computation of all the dyadic and scalar periodic Green's functions can be accelerated through the Ewald summation technique, as described in the next subsection.

4.1. Green's Function Calculation

The solution of the integral Equation (5) requires the computation of the Green's functions $\underline{\mathbf{G}}_A$ and G_V. For a periodic structure in free space, the dyadic magnetic vector potential Green's function is diagonal, i.e., $\underline{\mathbf{G}}_A = \mu_0 \left(\mathbf{u}_x \mathbf{u}_x G_{\mathrm{p}} + \mathbf{u}_y \mathbf{u}_y G_{\mathrm{p}} + \mathbf{u}_z \mathbf{u}_z G_{\mathrm{p}} \right)$, while the scalar electric potential Green's function is $G_V = G_{\mathrm{p}} / \varepsilon_0$. Thus, the solution of the EM problem in the 2-D periodic structure under analysis requires the efficient and accurate computation of the periodic Green's function $G_{\mathrm{p}}(\mathbf{r})$ only. However, the simple spatial representation of the 2-D free-space periodic Green's function G_{p} has the form of the very slowly converging double series [25, 26]

$$G_{\mathrm{p}}\left(\mathbf{r}, \mathbf{r}'\right) = \frac{1}{4\pi} \sum_{n=-\infty}^{n=+\infty} \sum_{m=-\infty}^{m=+\infty} \frac{e^{-jk_0 R_{mn}}}{R_{mn}} e^{-j\boldsymbol{\beta}_{\mathrm{t}}^{\mathrm{inc}} \cdot \boldsymbol{\rho}_{mn}} \tag{6}$$

where $k_0 = 2\pi/\lambda_0$ is the free-space wavenumber and

$$\boldsymbol{\beta}_{\mathrm{t}}^{\mathrm{inc}} = \beta_x^{\mathrm{inc}} \mathbf{u}_x + \beta_y^{\mathrm{inc}} \mathbf{u}_y \tag{7a}$$

$$\boldsymbol{\rho}_{mn} = np_x \cos\phi \, \mathbf{u}_x + \left[mp_s + np_x \sin\phi \right] \, \mathbf{u}_y \tag{7b}$$

$$\begin{aligned} R_{mn} &= \left| \mathbf{r} - \mathbf{r}_{mn} \right| \\ &= \sqrt{\left(u - np_x \cos\phi \right)^2 + \left(v - mp_s - np_x \sin\phi \right)^2 + w^2} \end{aligned} \tag{7c}$$

In (7), β_x^{inc} and β_y^{inc} are the x and y (transverse) components of the phase vector $\boldsymbol{\beta}^{\mathrm{inc}}$ of the incident plane wave, whereas $u = x - x'$, $v = y - y'$ and $w = z - z'$ are the three projections along the principal axes of the distance $\mathbf{R} = |\mathbf{r} - \mathbf{r}'|$ between the observation point $\mathbf{r} = (x, y, z)$ and the source point $\mathbf{r}' = (x', y', z')$ in the $(0, 0)$ unit cell.

It is evident that the spatial representation of the 2-D periodic Green's function in (6) has a very slow convergence, since the terms in the summation (6) decay as $O(1/m)$ as $m \to \infty$ and $O(1/n)$ as $n \to \infty$. To accelerate the calculation of the 2-D periodic Green's function, the Poisson's transformation is first applied to produce the equivalent and alternative expression

$$G_{\mathrm{p}}\left(\mathbf{r},\mathbf{r}'\right) = \frac{1}{2jA}\sum_{n=-\infty}^{n=+\infty}\sum_{m=-\infty}^{m=+\infty}\frac{e^{-jk_z(m,n)|z|}}{k_z\left(m,n\right)}e^{-j\,\mathbf{k}_{\mathrm{t}}(m,n)\cdot(\boldsymbol{\rho}-\boldsymbol{\rho}')} \tag{8}$$

where

$$\mathbf{k}_{\mathrm{t}}\left(m,n\right) = \mathbf{u}_x\left[\beta_x^{\mathrm{inc}} + 2\pi\left(\frac{n}{p_y\cos\phi} - \frac{m\sin\phi}{p_s\cos\phi}\right)\right] + \mathbf{u}_y\left(\beta_y^{\mathrm{inc}} + \frac{2\pi}{p_s}m\right) \tag{9a}$$

$$k_z(m,n) = \sqrt{k_0^2 - \mathbf{k}_{\mathrm{t}}\left(m,n\right)\cdot\mathbf{k}_{\mathrm{t}}\left(m,n\right)} \tag{9b}$$

while $\boldsymbol{\rho}$ and $\boldsymbol{\rho}'$ are the vectorial projections of the observation and source points on the transverse xy-plane, respectively, and $A = p_y p_s\cos\phi$ is the area of the unit cell. The representation in (8), known as *spectral representation*, is exponentially convergent, except for observation points close to the source plane. In the latter cases, the convergence is extremely slow and, in order to accelerate the calculation of the 2-D periodic Green's function, the Ewald summation technique is adopted [27], since it efficiently combines the spatial (6) and the spectral (8) representations to obtain a final expression of the 2-D periodic Green's function as a sum of two Gaussian fast decaying convergent series. In particular, the 2-D periodic Green's function can be expressed as $G_{\mathrm{p}} = G_{\mathrm{spat}} + G_{\mathrm{spect}}$. The *modified spatial series* is given by

$$G_{\mathrm{spat}} = \frac{1}{8\pi}\sum_{n=-\infty}^{n=+\infty}\sum_{m=-\infty}^{m=+\infty}\frac{e^{-j\boldsymbol{\beta}_{\mathrm{t}}^{\mathrm{inc}}\cdot\boldsymbol{\rho}_{mn}}}{R_{mn}} \cdot\left[e^{-jk_0R_{mn}}\mathrm{erfc}\left(R_{mn}E - \frac{jk_0}{2E}\right) + e^{+jk_0R_{mn}}\mathrm{erfc}\left(R_{mn}E + \frac{jk_0}{2E}\right)\right], \tag{10}$$

while the *modified spectral series* is given by

$$G_{\mathrm{spect}} = \frac{1}{4jA}\sum_{n=-\infty}^{n=+\infty}\sum_{m=-\infty}^{m=+\infty}\frac{e^{-j\mathbf{k}_{\mathrm{t}}(m,n)\cdot(\boldsymbol{\rho}-\boldsymbol{\rho}')}}{k_z\left(m,n\right)} \cdot\left[e^{-jk_z|w|}\mathrm{erfc}\left(\frac{jk_z}{2E} - |w|\,E\right) + e^{+jk_z|w|}\mathrm{erfc}\left(\frac{jk_z}{2E} + |w|\,E\right)\right], \tag{11}$$

where erfc(·) is the complementary error function. An efficient algorithm for the evaluation of the complementary error function with complex argument is reported in [28]. The real number E is the splitting parameter of the Ewald method and it is usually chosen by balancing the rate of decay of the two series in order to minimize the total number of terms in (10) and (11) [29, 30]. For spatial periods smaller than one wavelength the optimum value is [29]

$$E_{\text{opt}} = \sqrt{\frac{\pi}{A}}\,. \tag{12}$$

4.2. MoM Solution

The integral Equation (5) is solved by using the MoM formulation with subdomain basis functions and a Galerkin testing procedure. The surface S of the individual element in the unit cell has been discretized through nonoverlapping triangles and the unknown electric current density $\mathbf{J}$ has been expanded by a set of N subdomain vector basis functions (BFs) $\mathbf{\Lambda}_i$ as

$$\mathbf{J}(\mathbf{r}) = \sum_{i=1}^{N} J_i \mathbf{\Lambda}_i(\mathbf{r})\,, \tag{13}$$

where J_i are unknown complex amplitudes. As BFs we used the first-order roof-top Rao-Wilton-Glisson basis functions [31], which provide a continuous normal and linear tangent (CN/LT) representation of the vector quantities and proved to be accurate and efficient [23]. Each BF is associated with one interior edge i of the mesh ($i = 1, \ldots, N$) and it is defined on the two triangles T_i^+ and T_i^- adjacent to such i-th edge as shown in Fig. 4. The BF can be expressed as

$$\mathbf{\Lambda}_i(\mathbf{r}) = \begin{cases} +\frac{\ell_i}{2A_i^+}\boldsymbol{\rho}_i^+(\mathbf{r}) & \mathbf{r} \text{ inside } \mathrm{T}_i^+ \\ -\frac{\ell_i}{2A_i^-}\boldsymbol{\rho}_i^-(\mathbf{r}) & \mathbf{r} \text{ inside } \mathrm{T}_i^- \\ 0 & \text{elsewhere} \end{cases}, \tag{14}$$

where ℓ_i is the length of the i-th edge, $A_i^{\pm}$ are the areas of the surface triangular patches $\mathrm{T}_i^{\pm}$ and the vectors $\boldsymbol{\rho}_i^{\pm}$ connect the observation point $\mathbf{r}$ with the third free vertex of the plus/minus triangle.

Introducing the subdomain basis functions in Equation (5) and applying the Galerkin's test procedure, we obtain the final matrix equation of the problem as

$$[\mathbf{Z}]\ [\mathbf{J}] = [\mathbf{V}] \tag{15}$$

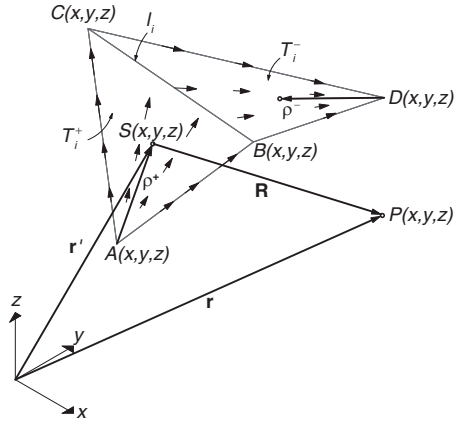

Figure 4. RWG basis functions.

where

$$Z_{ij} = j\omega \int_S \mathbf{\Lambda}_i(\mathbf{r}) \cdot \int_S \underline{\mathbf{G}}_A(\mathbf{r},\mathbf{r}') \cdot \mathbf{\Lambda}_j(\mathbf{r}')\,\mathrm{d}S'\mathrm{d}S + \frac{1}{j\omega} \int_S \nabla \cdot \mathbf{\Lambda}_i(\mathbf{r}) \int_S G_V(\mathbf{r},\mathbf{r}')\,\nabla \cdot \mathbf{\Lambda}_j(\mathbf{r}')\,\mathrm{d}S'\mathrm{d}S \quad (16a)$$

$$V_i = \int_S \mathbf{\Lambda}_i(\mathbf{r}) \cdot \mathbf{E}^{\mathrm{inc}}(\mathbf{r})\mathrm{d}S, \quad (16b)$$

and $\mathbf{J}$ is the vector of unknown complex amplitudes.

As concerns the integrations, the GF shows a singularity $1/R$ as the observation point $\mathbf{r}$ approaches the source point $\mathbf{r}'$ (i.e., $R \to 0$); in the proposed approach, such a singularity is extracted and analytical formulas [32] are used for the correct integration of the static 3-D GF times the vector BFs on the source triangles. Classical Gaussian quadrature rules are then used to compute all the remaining source and testing integrals [33].

A final remark concerns the MoM implementation for FSSs with PEC objects extending across the unit-cell boundaries. In such cases, the basis functions associated with the edges lying on the borders must allow the current to flow from one unit cell to the next. Floquet's theorem establishes that the currents on the periodic boundary of a surface mesh are related to the currents on the opposite periodic boundary through a phase relation. If the unknown current amplitude at an edge on one of the periodic boundaries is J_m, the value of the

current at the corresponding edge on the opposite periodic boundary is given by $J_m e^{j\boldsymbol{\beta}^{\mathrm{inc}}\cdot\mathbf{p}}$ [15]. This constraint is enforced in the MoM implementation adopting a symmetrical mesh on the opposite borders of the unit cell. The basis functions associated with opposite edges are joined to create only one unknown in the MoM system [18]. In this way, we end up with a complex-valued basis function which crosses the border, being partially defined on the triangle belonging to one edge and partially on the triangle belonging to the opposite edge, linearly independent from the others.

5. NUMERICAL RESULTS

To assess the suitability of the proposed structure in the frequency range below 1 GHz, we have computed the reflection coefficient Γ of the doubly periodic quadrifilar spiral apertures surface with the geometrical parameters reported in Table 1. All the structures are electrically small: in fact the period p ranges around 10 mm: at the maximum frequency of 1 GHz, the ratio between the maximum structure dimension and the wavelength is about 1/30. The results confirm that this type of doubly periodic elements shows a strong sub-wavelength response.

Table 1 summarizes the main features of the reflection coefficients of the periodic structures as functions of geometrical parameters and spiral segments number: the resonant frequency f_r, the BW computed at a level equal to 20 dB, and the relevant FBW.

Table 1. Influence of geometrical parameters and number of spiral segments on resonant frequency, bandwidth and fractional bandwidth.

Structure	w [mm]	g [mm]	p [mm]	N	f_r [GHz]	BW [GHz]	FBW [%]
#1	0.10	0.10	11.00	14	0.395	0.042	10.81
#2	0.15	0.10	10.75	11	0.522	0.052	10.09
#3	0.20	0.10	10.50	9	0.664	0.063	9.51
#4	0.10	0.15	10.75	11	0.493	0.061	12.41
#5	0.10	0.20	10.50	9	0.602	0.082	13.63
#6	0.10	0.30	10.80	7	0.737	0.113	15.40

Figure 5(a) shows the comparison among the reflection coefficients under a TEM impinging wave ($\alpha = 0°$, $\theta^{\mathrm{inc}} = 0°$ and $\phi^{\mathrm{inc}} = 90°$) of

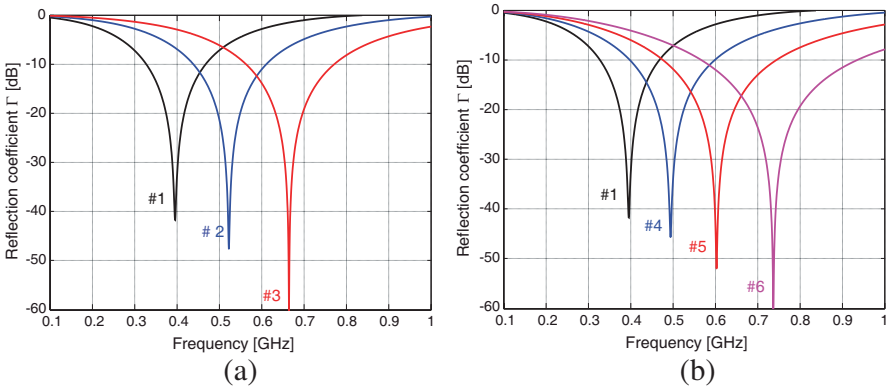

Figure 5. Reflection coefficient Γ as function of (mainly) (a) arm width w and (b) arm spacing g.

the first three structures denoted in Table 1 as #1, #2, and #3 whose main difference is the width w. It should be noted that the number of counter-woven segments N reduces by increasing w in order to keep the period p almost constant.

In addition, Fig. 5(b) shows the comparison among structures #1, #4, #5, and #6 characterized by an increasing spacing g. Even in this case the period p is kept almost constant, by reducing progressively the number of segments N. All the relevant geometrical parameters have been chosen in order to have a resonant frequency f_r below 1 GHz. In particular, it is possible to note that the increase of the width w from 0.1 mm to 0.2 mm leads to higher resonant frequencies, (from 395 MHz to 664 MHz) and to a (small) reduction of the FBW from 35.31% to 31.24%, respectively. On the contrary, the increase of the spacing g from 0.1 to 0.3 mm still leads to higher resonant frequencies (from 395 MHz to 737 MHz), but also significantly increases the relevant FBW (from 35.31% to 49.88%, respectively).

The results have been fully validated by means of two commercial codes: CST based on the Finite Integration Technique in the Time Domain and HFSS based on the Finite Element method in the Frequency Domain [34, 35]. Fig. 6 shows the comparison among the reflection coefficients Γ of the structures #1 and #6 (only these two FSS are considered for the sake of conciseness) computed either by the proposed MoM procedure and by the aforementioned codes. The agreement is excellent.

In Figs. 7(a) and 7(b), the sensitivity of BW and FBW with respect to incidence angle variations is reported considering TE- ($\alpha =$

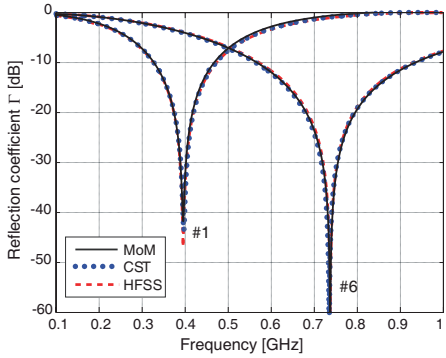

Figure 6. Comparison among the reflection coefficients Γ of structures #1 and #6 computed with the proposed MoM procedure and the commercial codes CST and HFSS.

90° and $\phi^{\text{inc}} = 90°$) or TM-polarized ($\alpha = 0°$ and $\phi^{\text{inc}} = 90°$) plane waves, respectively. It should be noted that both BW and FBW increase with the angle of incidence.

Theoretically, when the spatial periods are much lower than the wavelength, the behaviour of an FSS can be predicted by an equivalent surface impedance Z_s that is homogeneous, i.e., independent of the spatial position on the plane. Nevertheless, the analytical expression of the surface impedances can be carried out only in simple configurations (e.g., 1-D array of wires, 2-D array of patches or apertures), being the results of complex homogenization techniques [36–38]. The surface impedance provides an equivalent circuit representation of the FSS that is commonly used for the analysis. When the analytical expression of the surface impedance is not available, an approximate equivalent circuit model can still be obtained adopting extraction techniques directly on the results of measurements or full-wave numerical simulations. Yet, the values of the lumped elements in the equivalent circuit are valid only for the particular geometric configuration and incidence angle of the impinging wave that have been considered.

In the plane-wave incidence problem, the spiral-aperture array can be represented by a LC circuit with a shunt reactance composed of an inductance L and a capacitance C connected in parallel, as shown in Fig. 8. The equivalent shunt impedance L has been computed using the extraction technique described in [39–42] passing through the Z-parameters of the structure, easily obtained from the S-parameters. Fig. 9 shows the comparison between Z- and S-parameters computed through the MoM code and the relevant parameters obtained from

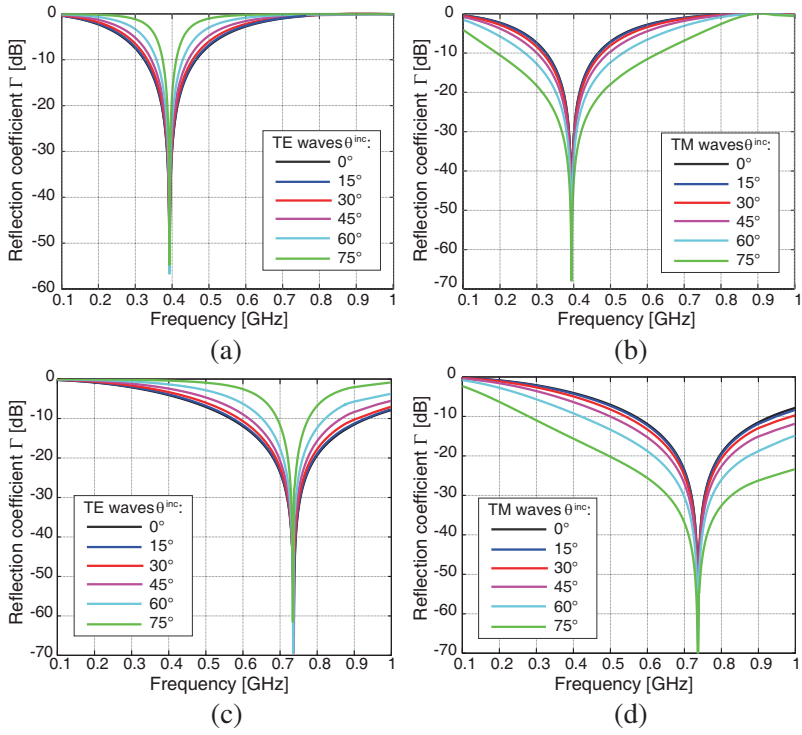

Figure 7. Reflection coefficient Γ ((a) and (b) structure #1, (c) and (d) structure #6) as a function of the angle of incidence for TE and TM-polarization.

the equivalent circuit extracted for the structure #1. The L and C parameters retrieved from the simulation of the structure #1 have the values $L = 83.237\,\text{nH}$ and $C = 1.936\,\text{pF}$, respectively. The S-parameters of the shunt-thru two-terminal component can be computed as

$$S_{\text{shunt}} = \frac{1}{Y_{\text{FSS}} + 2Y_0} \begin{bmatrix} -Y_{\text{FSS}} & 2Y_0 \\ 2Y_0 & -Y_{\text{FSS}} \end{bmatrix} \tag{17}$$

where $Y_{\text{FSS}} = [Z_{\text{FSS}}]^{-1}$ is the equivalent shunt admittance. Although the simple equivalent-circuit model gives only a basic description of artificial surfaces with complex unit-cell geometries (such as the doubly periodic array of entwined quadrifilar spiral apertures), it allows a fairly accurate guess of the FSS response near the fundamental resonance and provides qualitative insights into the principal features of the resonant structure.

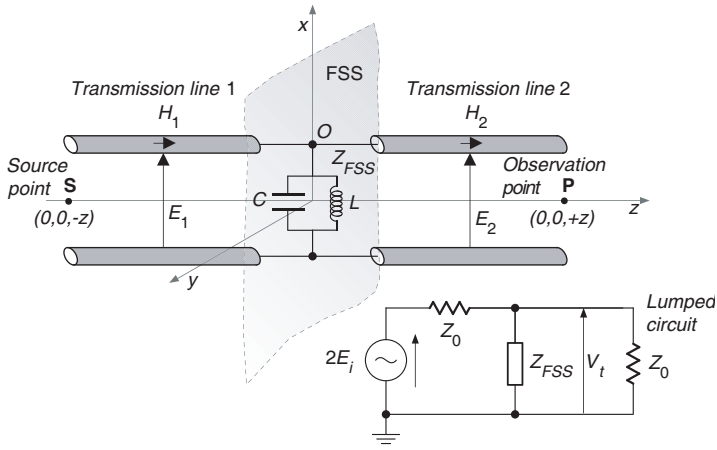

Figure 8. Approximate equivalent circuit modeling of the FSS in the surrounding medium, represented by means of transmission lines (or by its characteristic impedance, Z_0).

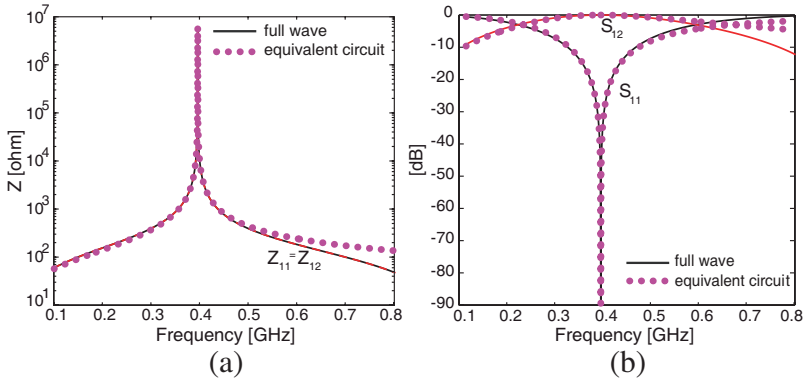

Figure 9. Frequency trends of (a) Z- and (b) S-parameters computed through the full-wave MoM code or the equivalent circuit shown in Fig. 8.

Successively, the FSS structures #2 and #4 of Table 1 have been used to design an absorber for the first resonant frequency of the shielded box shown in the inset of Fig. 1. The absorber configuration is shown in Fig. 10: it is a dielectric multilayered structure comprised of the two piled up dielectric slabs (dielectric #1 and #3) with the first FSS structure (FSS #2) placed on the surface between them and

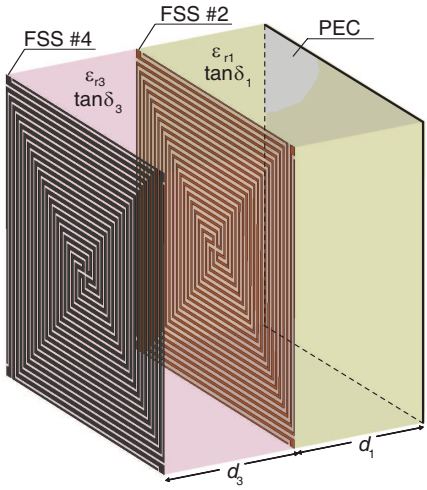

Figure 10. Configuration of the proposed absorber, realized by means of two dielectric layers and two entwined spiral aperture FSSs.

the second FSS structure (FSS #4) placed on the top surface. The continuous PEC plate placed at the bottom represents, generally with good approximation, the walls of the box. The use of two closely interacting FSSs is instead suggested in order to easily match the resonant frequency of the field which needs to be damped. In this connection, the FSS #4 is assumed to be perfectly conducting while the FSS #2 is characterized by a finite conductivity (i.e., it is a lossy FSS). In particular, the parameters of the designed absorber are as follows: $\varepsilon_{r1} = 10$, $\varepsilon_{r3} = 4.2$, $\tan\delta_1 = \tan\delta_3 = 0.025$, $d_1 = d_3 = 4\,\text{mm}$. Finally, the FSS #2 is formed by a resistive sheet with surface resistance equal to $150\,\Omega/\square$.

From Fig. 11 it is possible to note that the absorber is effective exactly at the first resonant frequency of the shielded enclosure and that its performance is reasonable compared to its geometrical dimensions. The proposed FSSs included into the absorber are able to absorb an EM field whose wavelength is about 50 times greater than its spatial period p. Moreover, the absorbing performance are not too much degraded by increasing the angle of incidence θ_{inc}, as shown in Fig. 11. Nevertheless, a larger bandwidth would be useful to damp also higher-order resonant modes: an ongoing research is currently conducted to improve the BW, exploiting multi-resonances.

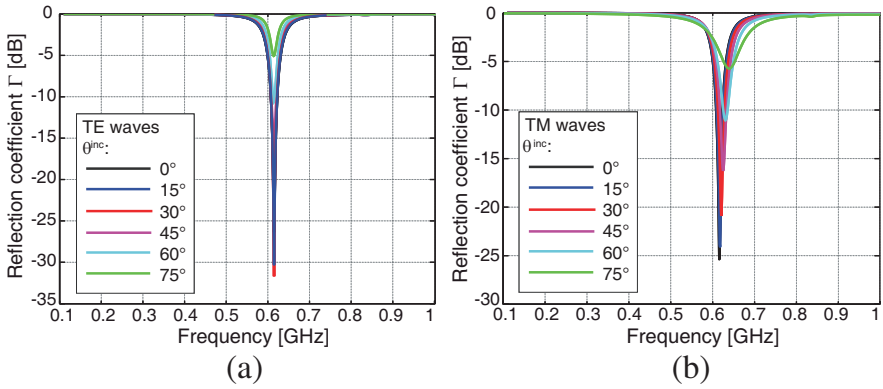

Figure 11. Reflection coefficient Γ of the proposed absorber configuration as function of the incidence angle, for (a) TE- and (b) TM-polarization.

6. CONCLUSIONS

In this work, a new intertwined spiral-aperture frequency-selective surface is proposed for the design of polarization-insensitive metamaterial absorbers that operate below 1 GHz, where the first resonances of small commercial enclosures take place. The presented results show that the proposed FSS has a strong sub-wavelength response, enhanced by the dielectric substrate, which is suitable for the design of compact planar absorbers with excellent angular and polarization stability. Finally, a compact and light-weight absorbing material based on these novel FSSs is presented and its EM behavior analyzed.

APPENDIX A.

Actual enclosures generally present a number of apertures of different shapes. The absorbers used to line the internal sides of actual enclosures must conform with the apertures. To this end, the proposed FSS geometry may be adapted preserving the main features of the configuration, as shown in Fig. A1: in the example, one unit cell has been removed and the arms of neighboring spiral apertures are connected in order to retain apertures intertwining. In case of apertures wider than one unit cell, a similar adaptation may be also considered.

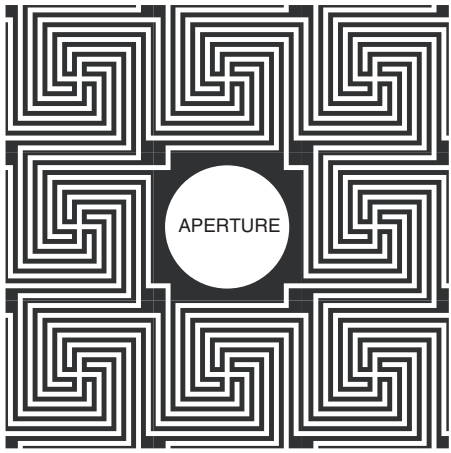

Figure A1. Adaption of the proposed absorber's geometry to a possible aperture a wall of the enclosure.

REFERENCES

1. Luo, M. and K.-M. Huang, "Prediction of the electromagnetic field in metallic enclosures using artificial neural networks," *Progress In Electromagnetics Research*, Vol. 116, 171–184, 2011.
2. Dehkhoda, P., A. Tavakoli, and R. Moini, "Fast calculation of the shielding effectiveness for a rectangular enclosure of finite wall thickness and with numerous small apertures," *Progress In Electromagnetics Research*, Vol. 86, 341–355, 2008.
3. Wang, Y. J., W. J. Koh, C. K. Lee, and K. Y. See, "Electromagnetic coupling analysis of transient signal through slots or apertures perforated in a shielding metallic enclosure using FDTD methodology," *Progress In Electromagnetics Research*, Vol. 36, 247–264, 2002.
4. Nie, X.-C. and N. Yuan, "Accurate modeling of monopole antennas in shielded enclosures with apertures," *Progress In Electromagnetics Research*, Vol. 79, 251–262, 2008.
5. Lei, J.-Z., C.-H. Liang, and Y. Zhang, "Study on shielding effectiveness of metallic cavities with apertures by combining parallel FDTD method with windowing technique," *Progress In Electromagnetics Research*, Vol. 74, 82–112, 2007.
6. Wang, Y. J., W. J. Koh, and C. K. Lee, "Coupling cross section and shielding effectiveness measurements on a coaxial cable by both mode-tuned reverberation chamber and GTEM cell

methodologies," *Progress In Electromagnetics Research*, Vol. 47, 61–73, 2004.

7. Araneo, R. and S. Celozzi, "Analysis of the shielding performance of ferromagnetic screens," *IEEE Trans. Magn.*, Vol. 39, No. 2, 1046–1052, Mar. 2003.
8. Marvin, A. C., J. F. Dawson, S. Ward, L. Dawson, J. Clegg, and A. Weissenfeld, "A proposed new definition and measurement of the shielding effect of equipment enclosures," *IEEE Trans. Electromagn. Compat.*, Vol. 46, No. 3, 459–468, Aug. 2004.
9. Celozzi, S., "New figures of merit for the characterization of the performance of shielding enclosures," *IEEE Trans. Electromagn. Compat.*, Vol. 46, No. 1, 142, Feb. 2004.
10. Araneo, R. and S. Celozzi, "Toward a definition of the shielding effectiveness in the time-domain," *Proc. IEEE Electromagn. Compat. Symp.*, 113–117, Aug. 5–9, 2013.
11. Iqbal, M. N., F. F. B. A. Malek, S. H. Ronald, M. S. Bin Mezan, K. M. Juni, and R. Chat, "A study of the EMC performance of a graded-impedance, microwave, rice-husk absorber," *Progress In Electromagnetics Research*, Vol. 131, 19–44, 2012.
12. Chung, B.-K. and H.-T. Chuah, "Modeling of RF absorber for application in the design of anechoic chamber," *Progress In Electromagnetics Research*, Vol. 43, 273–285, 2003.
13. Huang, L. and H. Chen, "Multi-band and polarization insensitive metamaterial absorber," *Progress In Electromagnetics Research*, Vol. 113, 103–110, 2011.
14. Zhang, J.-C., Y.-Z. Yin, and J.-P. Ma, "Design of narrow band-pass frequency selective surfaces for millimeter wave applications," *Progress In Electromagnetics Research*, Vol. 96, 287–298, 2009.
15. Su, J., X.-W. Xu, M. He, and K. Zhang, "Integral-equation analysis of frequency selective surfaces using Ewald transformation and lattice symmetry," *Progress In Electromagnetics Research*, Vol. 121, 249–269, 2011.
16. Hosseini, M., A. Pirhadi, and M. Hakkak, "A novel AMC with little sensitivity to the angle of incidence using 2-layer Jerusalem cross FSS," *Progress In Electromagnetics Research*, Vol. 64, 43–51, 2006.
17. Li, L., Y. Yang, and C. Liang, "A wide-angle polarization insensitive ultra-thin metamaterial absorber with three resonant modes," *J. Appl. Phys.*, Vol. 110, No. 6, 063702–063702-5, 2011.
18. Araneo, R., G. Lovat, and S. Celozzi, "Shielding effectiveness of periodic screens against finite high-impedance near-field sources,"

IEEE Trans. Electromagn. Compat., Vol. 53, No. 3, 706–716, Aug. 2011.

19. Araneo, R. and G. Lovat, "An efficient MoM formulation for the evaluation of the shielding effectiveness of rectangular enclosures with thin and thick apertures," *IEEE Trans. Electromagn. Compat.*, Vol. 50, No. 2, 294–304, Mar. 2008.
20. Araneo, R. and G. Lovat, "Fast MoM analysis of the shielding effectiveness of rectangular enclosures with apertures, metal plates, and conducting objects," *IEEE Trans. Electromagn. Compat.*, Vol. 51, No. 2, 274–283, Mar. 2009.
21. Vallecchi, A. and A. G. Schuchinsky, "Entwined planar spirals for artificial surfaces," *IEEE Antennas Wireless Propagat. Lett.*, Vol. 9, 994–997, Jul. 2010.
22. Vallecchi, A. and A. G. Schuchinsky, "Artificial surfaces formed by tessellations of intertwined spirals," *Proc. 5th European Conf. Antennas Propag.*, Vol. 7, 1846–1848, Apr. 2011.
23. Peterson, A. F., S. L. Ray, and R. Mittra, *Computation Methods for Electromagnetics*, IEEE Press, Piscataway, NJ, 1998.
24. Mosig, J. R., "Integral equation technique," *Numerical Techniques for Microwave and Millimeter Wave Passive Structures*, T. Itoh, Ed., Wiley, New York, 1989.
25. Bladel, J. G. V., *Electromagnetic Fields*, IEEE Press, Piscataway, NJ, 2007.
26. Celozzi, S., R. Araneo, and G. Lovat, *Electromagnetic Shielding*, Wiley-IEEE, Hoboken, 2008.
27. Jordan, K. E., G. R. Richter, and P. Sheng, "An efficient numerical evaluation of the Green's function for the Helmholtz operator on periodic structures," *J. Comput. Phys.*, Vol. 63, No. 1, 222–235, Mar. 1986.
28. Weideman, J. A. C., "Computation of the complex error function," *SIAM J. Numer. Anal.*, Vol. 31, No. 5, 1497–1518, Oct. 1994.
29. Kustepeli, A. and A. Q. Martin, "On the splitting parameter in the Ewald method," *IEEE Microwave Guided Wave Lett.*, Vol. 10, No. 5, 168–170, 2000.
30. Lovat, G., P. Burghignoli, and R. Araneo, "Efficient evaluation of the three-dimensional periodic Green's function through the Ewald method," *IEEE Trans. Microwave Theory Tech.*, Vol. 56, No. 9, 2069–2075, 2008.
31. Rao, S. M., D. R. Wilton, and A. W. Glisson, "Electromagnetic scattering by surfaces of arbitrary shape," *IEEE Trans. Antennas*

Propagat., Vol. 30, No. 3, 409–418, May 1988.

32. Graglia, R. D., "On the numerical integration of the linear shape functions times the 3-D Green's function or its gradient on a plane triangle," *IEEE Trans. Antennas Propagat.*, Vol. 41, No. 10, 1448–1455, Oct. 1993.
33. Dunavant, D. A., "High degree efficient symmetrical Gaussian quadrature rules for the triangle," *Intern. J. Num. Meth. Engin.*, Vol. 21, 1129–1148, Jun. 1985.
34. Microwave Studio Computer Simulation Technology (CST), 2013, http://www.cst.de.
35. HFSS (ANSYS), 2013, http://www.ansys.com.
36. Wu, K., *Frequency Selective Surfaces and Grid Array*, Wiley, New York, 1995.
37. Munk, B. A., *Frequency Selective Surfaces: Theory and Design*, Wiley, New York, 2000.
38. Cheng, Y., Y. Wang, Y. Niea, R. Z. Gong, X. Xiong, and X. Wang, "Design, fabrication and measurement of a broadband polarization insensitive metamaterial absorber based on lumped elements," *J. Appl. Phys*, Vol. 111, No. 4, 044902–044902-4, 2012.
39. Araneo, R., "Extraction of broadband passive lumped equivalent circuits of microwave discontinuities," *IEEE Trans. Microwave Theory Tech.*, Vol. 54, No. 1, 393–401, 2006.
40. Wang, R., J. Xu, C. L. Wei, M.-Y. Wang, and X.-C. Zhang, "Improved extraction of coupling matrix and unloaded Q from S-parameters of lossy resonator filters," *Progress In Electromagnetics Research*, Vol. 120, 67–81, 2011.
41. Araneo, R., C. Wang, X. Gu, S. Celozzi, and J. Drewniak, "Differential signalling in PCBs: Modeling and validation of dielectric losses and effects of discontinuities," *Proc. IEEE Electromagn. Compat. Symp.*, Vol. 2, 933–938, Aug. 13–17, 2001.
42. Araneo, R., C. Wang, X. Gu, J. Drewniak, and S. Celozzi, "Efficient modeling of discontinuities and dispersive media in printed transmission lines," *IEEE Trans. Magn.*, Vol. 38, No. 2, 765–768, Mar. 2002.